Title

Circuit-level design principles for transmission-mode microwave impedance microscopy

Journal

Applied Physics Letters, 122(12)

ISSN

0003-6951

Authors

Shan, Jun-Yi
Morrison, Nathaniel
Y., Eric

Publication Date

2023-03-20

DOI

10.1063/5.0143247

Circuit-level design principles for transmission-mode microwave impedance microscopy

Jun-Yi Shan,[1,2] Nathaniel Morrison,[1] and Eric Y. Ma[1,2,a)]
[1)] *Department of Physics, University of California, Berkeley, Berkeley, CA 94720, USA*
[2)] *Lawrence Berkeley National Laboratory, Berkeley, CA 94720, USA*

The recently developed technique of transmission-mode microwave impedance microscopy (T-MIM) has greatly extended the capabilities of standard reflection-mode MIM to novel applications such as the *in-operando* study of nanoscale electro-acoustic devices. As is common for new techniques, systematic design principles for boosting sensitivity and balancing bandwidth are lacking. Here we show numerically and analytically that the T-MIM signal is proportional to the *reflection-mode* voltage enhancement factor η of the circuit, as long as the output impedance of the local voltage source is properly treated. We show that this proportionality holds in the currently achievable "weak sampling" regime and beyond, for which we demonstrate a realistic path with commercially available superconducting components and critically coupled impedance matching networks. We demonstrate that for these next-generation designs, the sensitivity is generally maximized at a slightly different frequency from the unloaded S_{11} resonance, which can be explained by the maximum power transfer theorem.

Electro-acoustic devices based on surface acoustic waves (SAWs) and Lamb waves are essential for wireless communication and sensing applications, with small form factors due to the slow speed of sound and convenient piezoelectric electromechanical transduction. Recently, acoustic waves have also been shown to couple to superconducting qubits[1] and spins[2], control photons[3] and electrons[4], and exhibit topological characteristics[5]. As increasingly high frequencies are used in such applications[6], imaging the wave dynamics in these devices with nanoscale spatial resolution, especially *in-operando*, has become a grand challenge.

A recent breakthrough is the demonstration of transmission-mode microwave impedance microscopy (T-MIM)[7,8] that can image nanoscale distributions of the electric potentials accompanied by acoustic waves at up to 6 GHz with sub-100 nm spatial resolution, all in a working device. It has been used to visualize wave propagation in phononic circuits[9,10], to demonstrate electrical control of SAWs[11], and to resolve topological edge states in phononic crystals[12,13]. In light of the increasing importance of the technique, a set of systematic circuit-level design principles for T-MIM – as we describe in this Letter – would be a timely addition to the literature and help to guide the development of this nascent technology.

MIM brings microwave sensing capabilities to a scanning probe microscope[14]. Conventional MIM is performed in the reflection mode (herein refered to as R-MIM for clarity), where an ultrasensitive microwave reflectometer measures variations in the tip-sample admittance caused by nanoscale inhomogeneities in the complex permittivity of the sample[15] (Fig. 1a). In R-MIM, an impedance matching network is commonly inserted between the reflectometer and the probe to maximize power delivery and to increase sensitivity. Indeed, we showed in an earlier work[16] that the R-MIM signal depends *quadratically* on the voltage enhancement factor of the circuit $\eta = V^{\mathrm{R}}_{\mathrm{probe}}/V^{\mathrm{R}}_{\mathrm{in}}$, where $V^{\mathrm{R}}_{\mathrm{probe}}$ is the voltage at the probe and $V^{\mathrm{R}}_{\mathrm{in}}$ is the amplitude of the incident microwave going into the matching network (superscripts indicate reflection mode). A strong signal can thus be achieved near the resonance of a high quality-factor (Q-factor) resonator-style matching network at the cost of bandwidth, but the proportionality holds both on- and off-resonance for any matching network design.

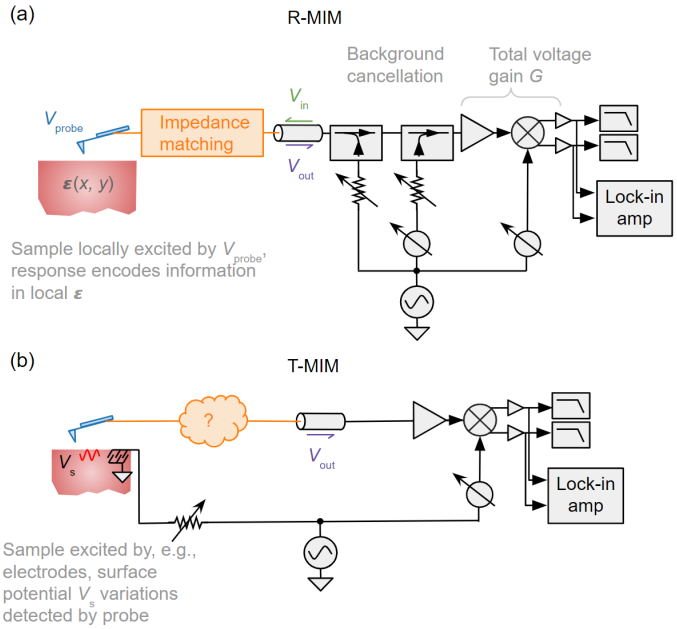

FIG. 1. (a) Schematic of R-MIM. A microwave source delivers microwave fields to the sample surface through an impedance matching network and the probe, and the reflected microwave is background-corrected, amplified, and detected with an in-phase and quadrature (IQ) mixer. (b) Schematic of T-MIM. A microwave source excites a device through, e.g., an IDT. The surface electric potential V_{s} is picked up by the probe and detected after passing through an intermediate circuit to be optimized in this work.

The operation of T-MIM is fundamentally different. The microwave source excites the sample, such as a SAW filter, separately from the probe, e.g., by launching a SAW with an inter-digital transducer (IDT). The electric potential propagat-

[a)] Electronic mail: eric.y.ma@berkeley.edu

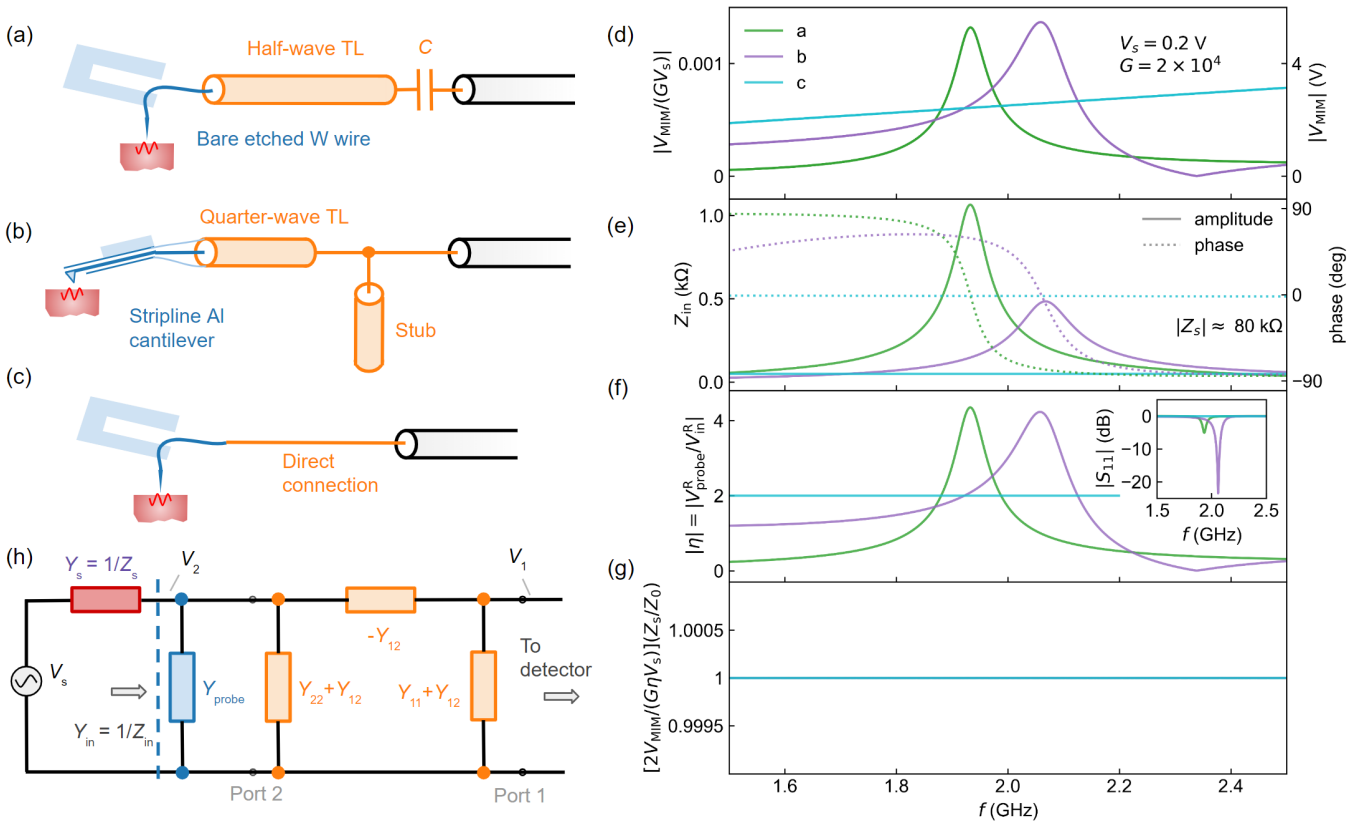

FIG. 2. (a)-(c) The schematics of three distinct T-MIM designs: (a) etched bare metal probe with half-wave resonator matching, (b) stripline cantilever probe with quarter-wave and stub matching, and (c) etched bare metal probe with direct connection. The light blue shades represent the quartz tuning fork for topography feedback in (a) and (c), and the probe carrier chip in (b). The red shades represent the samples. (d) Normalized (left axis) and absolute (right axis) T-MIM signal V_{MIM} between 1.5 GHz and 2.5 GHz for the three different designs. (e) Load impedance Z_{in} looking from the sample into the probe. (f) Voltage enhancement factor $|\eta|$, defined in the R-MIM geometry. The inset shows the $|S_{11}|$ looking into the matching network. (g) The dimensionless quantity $[2V_{MIM}/(G\eta V_s)](Z_s/Z_0)$. (h) Equivalent diagram of a T-MIM circuit that is linear and reciprocal.

ing with the SAW is then picked up by the probe, which acts as a nano-antenna (Fig. 1b). Therefore, T-MIM measures the potential profile in a working device instead of the intrinsic complex permittivity of the sample. On the circuit level, distinct from R-MIM, the microwave only travels one-way from the sample to the homodyne detector through the matching network. One would thus expect a different relationship between the T-MIM signal and the properties of the matching-network-probe circuitry.

More specifically, a complete T-MIM circuit has two types of parameters: one set is determined by the matching-network-probe design and is shared between transmission and reflection modes; another set is unique to transmission-mode operation. The former includes the voltage enhancement factor η and the complex reflection coefficient S_{11}, the one-port S-parameter that characterizes the quality of the impedance matching looking into the matching network. The latter includes the surface source potential V_s and the effective source output impedance Z_s. In the electro-quasistatic limit, applicable here since the tip is much smaller than the relevant microwave wavelength, V_s is simply divided between Z_s and the "load impedance" Z_{in}, the input impedance looking into the probe (Fig. 2h).

We first simulated three distinct T-MIM designs to gain numerical insights (Fig. 2). Fig. 2a shows a tuning fork sensor with an etched tungsten wire probe and a half-wave transmission line (TL) resonator matching network. Fig. 2b shows a cantilever-based stripline aluminum probe with a quarter-wave and stub matching network. Fig. 2c shows a design with the same probe as in Fig. 2a, but with a direct connection to the detector. For each design, we performed a transmission-mode simulation to obtain the T-MIM signal V_{MIM} and the input impedance Z_{in}, and a reflection-mode simulation to obtain η and S_{11}. In the reflection-mode simulations, we included the source output impedance Z_s as a regular tip-sample interaction impedance in parallel with the probe (Fig. 2h). See Table I for the detailed simulation parameters.

The simulation results show that for resonator-type matching networks (Fig. 2a, b), V_{MIM} and $|\eta|$ follow similar frequency-dependent profiles with similar maximum values for cases a and b at their respective resonant frequencies (Fig. 2d, f), while the behaviors of Z_{in} and S_{11} differ markedly from V_{MIM} (Fig. 2e and 2f inset). In contrast, the direct connection case (Fig. 2c) shows broadband behavior and a lower max-

TABLE I. Simulation parameters.

$V_s = 0.2\,\mathrm{V}$, $G = 2\times10^4$, Z_s corresponds to a 1 fF capacitor[7]				
Case	Probe			Impedance matching
	R (Ω)	L(nH)	C (pF)	
(a)	Bare etched W wire with tuning fork[17]: $l = 3\,\mathrm{mm}$, $d = 80\,\mu\mathrm{m}$			Half-wave TL: FM-SR020CU-STR Fairview Microwave
	0.25	2.6	0.04	$l_{TL} = 57\,\mathrm{mm}$, $C = 0.17\,\mathrm{pF}$
(b)	Stripline Al cantilever[18]: 5-300N PrimeNano			Quarter-wave TL: FM-SR118CU-COIL Fairview Microwave
	5	0.5	1	$l_{TL} = 20.5\,\mathrm{mm}$, $l_{stub} = 24.5\,\mathrm{mm}$

imum V_{MIM}, although only by a factor of ~ 2. Note that in all these realistic cases, $|Z_{in}| \ll |Z_s|$, which results in "weak sampling", i.e., $V_{MIM}/G \ll V_s$.

The similarities in V_{MIM} and η suggest that they may be linearly related. Indeed, the complex dimensionless factor $[2V_{MIM}/(G\eta V_s)](Z_s/Z_0)$ is unity for all cases at all frequencies within numerical error (Fig. 2g).

Following this numerical insight, we set out to analytically derive this linear relationship between V_{MIM} and η, and to identify any corrections or necessary approximations. We start with the fact that any linear, reciprocal impedance matching network with an admittance matrix of

$$\hat{Y} = \begin{bmatrix} Y_{11} & Y_{12} \\ Y_{21} & Y_{22} \end{bmatrix}$$

can be modeled as a two-port π-shaped equivalent circuit (Fig. 2h)[19]. Thus, we can calculate the input admittance $Y_{in}(=1/Z_{in})$ as

$$\begin{aligned} Y_{in} &= Y_{probe} + Y_{22} + Y_{12} - \frac{Y_{12}(Y_{11}+Y_{12}+Y_0)}{-Y_{12}+Y_{11}+Y_{12}+Y_0} \\ &= Y_{probe} + Y_{22} - \frac{Y_{12}^2}{Y_{11}+Y_0}, \end{aligned}$$

where $Y_0 = 1/Z_0$ is the characteristic admittance of the system (Z_0 is generally $50\,\Omega$) and Y_{probe} is the probe admittance. Following the voltage division rule we obtain

$$V_2 = V_s \cdot Z_{in}/(Z_{in}+Z_s).$$

The T-MIM signal V_{MIM} is then

$$\begin{aligned} V_{MIM} &= GV_1 = GV_2 \frac{1/(Y_{11}+Y_{12}+Y_0)}{1/(Y_{11}+Y_{12}+Y_0) - 1/Y_{12}} \\ &= -GV_2 \frac{Y_{12}}{Y_{11}+Y_0} \qquad (1) \\ &= \frac{GV_sZ_0}{2Z_s} \cdot [-\frac{2Y_{12}Y_0}{(Y_s+Y_{22}+Y_{probe})(Y_0+Y_{11}) - Y_{12}^2}]. \end{aligned}$$

We note that the last fraction in Eq. 1 is precisely the R-MIM voltage enhancement factor $\eta = V_{probe}^R/V_{in}^R$ when the tip-sample interaction admittance is Y_s[16]. Therefore, we have

$$V_{MIM} = G \cdot \frac{Y_s}{2Y_0} \cdot \eta \cdot V_s, \qquad (2)$$

showing that the measured T-MIM signal is indeed proportional to η. Comparing with the R-MIM result[16] of

$$\Delta V_{MIM}^R = -G \cdot \frac{\Delta Y}{2Y_0} \cdot \eta^2 \cdot V_{in},$$

the linear, instead of quadratic, dependence on η here can be intuitively understood as the consequence of a single pass through the MIM circuits in T-MIM.

One conclusion we can draw from these results is that ultra-broadband operation is easier for T-MIM than for R-MIM. Two factors contribute here. First, the direct-connection design (Fig. 2c) has an $|\eta|$ of ~ 2, as opposed to ~ 1 for the Z_0 shunt matching for broadband R-MIM[16]. Second, the signal scales linearly instead of quadratically with η in T-MIM, so the loss in sensitivity compared with typical room-temperature narrow-band $|\eta|_{max}$ of up to ~ 10 is less significant.

For narrow-band, sensitivity-limited operation, Eq. 2 is a general result that can guide us beyond the "weak sampling" limit that has been assumed in literature so far[7], since we did not use the condition $|Z_{in}| \ll |Z_s|$ in our derivation. We note that given G, V_s, and Z_s, boosting V_{MIM} is equivalent to increasing the voltage enhancement factor η, which, as we will show below, benefits from low-loss and critically-coupled resonator-type matching networks, and is distinct from simply increasing $|Z_{in}|$ or optimizing S_{11} as suggested previously[7].

To this end, we take the design of a bare metal wire probe with a half-wave resonator matching network (Fig. 2a) as a model system and analyze how the TL loss and the coupling capacitance C affect the T-MIM performance. First, we set the TL loss to a lower value of $0.1\,\Omega$/m, which can be achieved using commercially available superconducting co-axial cables (such as COAX SC-086/50-NbTi-NbTi). We then carried out a series of simulations with C varying from 0.17 pF to 0.001 pF. The results show several features (Fig. 3). First, as C is reduced, the resonant frequency shifts and the resonances become generally narrower. Second, the peak V_{MIM}, $|\eta|$, and $|S_{11}|$ values first increase and then decrease (Fig. 3a, c). Third, the peak $|Z_{in}|$ increases monotonically and surpasses $|Z_s|$ for $C <\sim 0.05\,\mathrm{pF}$ (Fig. 3b). Fourth, Eq. 2 holds exactly in all cases, as expected (Fig. 3d).

The first two observations can be well understood within the framework of coupled resonators[20]. Because of the low TL loss, the total round-trip loss of the half-wave resonator

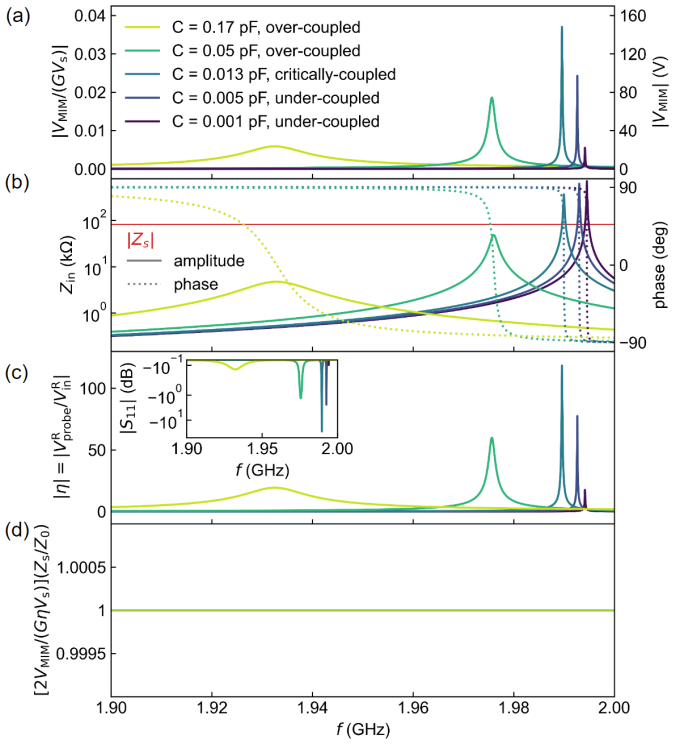

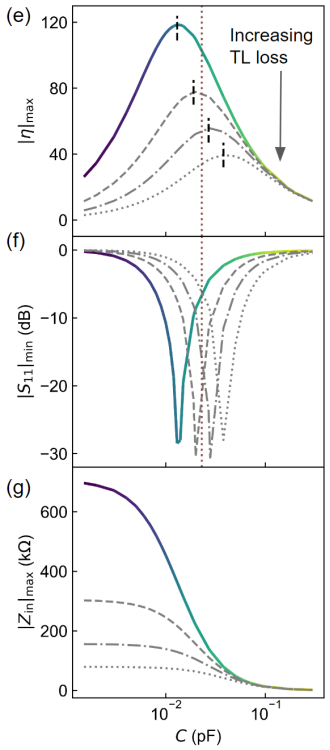

FIG. 3. (a) T-MIM signal V_{MIM} for representative coupling capacitor values using the design in Fig. 2a and low-loss TLs of $0.1\,\Omega/\mathrm{m}$. (b) Load impedance Z_{in}, looking from the sample into the probe. The red horizontal line marks $|Z_{\mathrm{s}}|$. (c) Voltage enhancement factor $|\eta|$. The inset shows the S_{11} looking into the matching network. (d) The dimensionless quantity $[2V_{\mathrm{MIM}}/(G\eta V_{\mathrm{s}})](Z_{\mathrm{s}}/Z_0)$. (e) The maximum $|\eta|$ as a function of the coupling capacitor value C for different TL losses. TL losses from top to bottom: 0.1, 0.25, 0.5, and $1\,\Omega/\mathrm{m}$. The analytically derived critically coupled C for each TL loss is indicated by short black vertical dashed lines. The TL loss used in Fig. 2 is $50\,\Omega/\mathrm{m}$. (f, g) Minimum $|S_{11}|$ and maximum $|Z_{\mathrm{in}}|$ as a function of the coupling capacitor value C for different TL losses.

is dominated by the coupling to the external circuits through the capacitor when $C >\sim 0.05\,\mathrm{pF}$. The system is thus *over-coupled*, leading to broad, shallow resonances and low enhancement factors. As C becomes smaller, the coupling loss decreases and eventually becomes similar to the intrinsic TL loss, at which point the system becomes *critically-coupled*, leading to a narrow and strong resonance with the best possible total coupling (S_{11}) and the highest possible enhancement factor and thus T-MIM signal. Finally, as C becomes even smaller, the system becomes *under-coupled*, leading to a narrow but shallow resonance and reduced voltage enhancement.

Indeed, if we plot the peak η and S_{11} values as a function of C for different TL losses (Fig. 3e, f), the peak positions agree very well with the C values that give rise to equal round-trip TL loss and capacitive coupling loss (short vertical dashed lines in Fig. 3e):

$$1-\exp(-\frac{2R'l_{\mathrm{TL}}}{Z_0}) = 4Z_0^2/(4Z_0^2+\frac{1}{C^2\omega^2}),$$

where R' is the resistance per unit length of the TL. Following the results for different TL losses in Fig. 3e and f, we can conclude that to maximize narrow-band sensitivity, one should choose components with the lowest possible loss first, and then tune the coupling strength to achieve critical coupling, using S_{11} as a convenient guide. On the other hand, following vertical cuts in Fig. 3e and f, we can conclude that if the coupling strength C needs to be fixed, one should *not* aim for critical coupling. Instead, it is preferable to lower the loss of the components as much as possible, even if it makes the system over-coupled and S_{11} worse (see supplementary materials for more details). These strategies are general because the concept of intrinsic loss and coupling loss can be readily applied to other resonator-type impedance matching networks[21].

Finally, we explain the apparent deviation between the trend of $|Z_{\mathrm{in}}|_{\mathrm{max}}$ and that of η and V_{MIM}, especially for under-coupled systems (Fig. 3g). From the simple voltage division of V_{s} between Z_{in} and Z_{s}, and the "weak sampling" limit of $|Z_{\mathrm{in}}| \ll |Z_{\mathrm{s}}|$, one might expect V_{MIM} to be correlated with Z_{in}, which then needs to be maximized. However, the voltage division only describes the voltage sampled by the *probe* (V_2 in Fig. 2h), instead of that coupled into the external detection circuit (V_1). Therefore, although a smaller C always leads to a larger $|Z_{\mathrm{in}}|_{\mathrm{max}}$ and thus V_2, it does so at the cost of reducing V_1 and thus V_{MIM} in under-coupled systems. In fact, if $|Z_{\mathrm{in}}|_{\mathrm{max}}$ is comparable to or larger than $|Z_{\mathrm{s}}|$, V_{MIM} is *not* maximized at the frequency f_0' that maximizes $|Z_{\mathrm{in}}|$. Instead, it is maximized at f_0 which makes Z_{in} the closest to Z_{s}^* (Fig. 4a, b). This is consistent with the maximum power transfer theorem[19]. Practically, because f_0' also minimizes the "unloaded" $|S_{11}|$ (i.e., with the probe away from the sample), there will be an offset between the result of an unloaded $|S_{11}|$ measurement and the actual optimal working frequency for T-MIM (Fig. 4c). This discrepancy persists for critically- and over-coupled systems, albeit less important due to the broader resonances (see supplementary materials).

SUPPLEMENTARY MATERIALS

See supplementary materials for the discussion of critical coupling conditions and the resonant frequency differences between unloaded S_{11} and V_{MIM}.

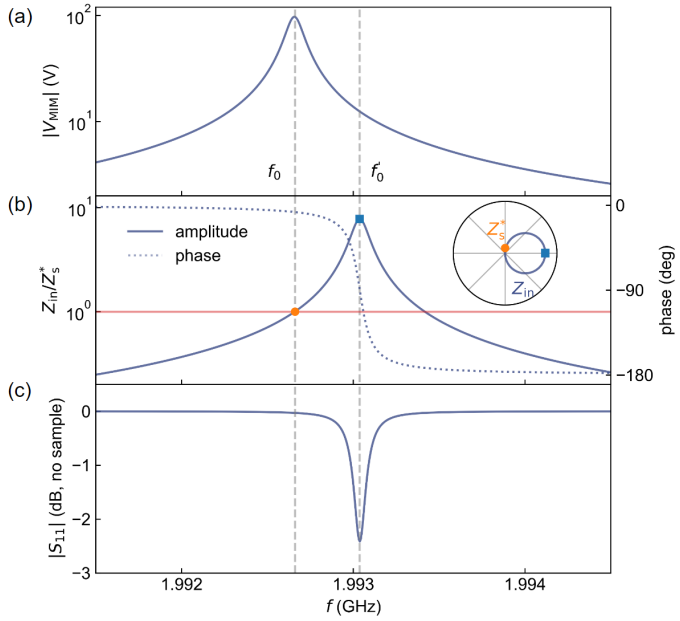

FIG. 4. (a) T-MIM signal V_{MIM} for the $C = 0.005\,\mathrm{pF}$ and low-loss TL case, plotted in a narrower frequency range. (b) The ratio between Z_{in} and the complex conjugate of the source impedance Z_{s}. The inset shows the polar plot of Z_{in}. The orange circle marks $Z_{\mathrm{in}}/Z_s^* \approx 1$. The blue square marks the maximum $|Z_{\mathrm{in}}|$. (c) "Unloaded" $|S_{11}|$ of the matching network and the probe, when the sample is not present. There is a frequency difference between the maxima of V_{MIM} and Z_{in}/Z_s^* or "unloaded" $|S_{11}|$.

ACKNOWLEDGMENTS

This work was supported by the Laboratory Directed Research and Development Program of Lawrence Berkeley National Laboratory under U.S. Department of Energy Contract No. DE-AC02-05CH11231.

DATA AVAILABILITY

The data that support the findings of this study are available from the corresponding author upon reasonable request.

REFERENCES

[1]Y. Chu, P. Kharel, W. H. Renninger, L. D. Burkhart, L. Frunzio, P. T. Rakich, and R. J. Schoelkopf, "Quantum acoustics with superconducting qubits," Science **358**, 199–202 (2017).

[2]S. J. Whiteley, G. Wolfowicz, C. P. Anderson, A. Bourassa, H. Ma, M. Ye, G. Koolstra, K. J. Satzinger, M. V. Holt, F. J. Heremans, A. N. Cleland, D. I. Schuster, G. Galli, and D. D. Awschalom, "Spin–phonon interactions in silicon carbide addressed by Gaussian acoustics," Nat. Phys. **15**, 490–495 (2019).

[3]K. Fang, M. H. Matheny, X. Luan, and O. Painter, "Optical transduction and routing of microwave phonons in cavity-optomechanical circuits," Nat. Photon. **10**, 489–496 (2016).

[4]S. Hermelin, S. Takada, M. Yamamoto, S. Tarucha, A. D. Wieck, L. Saminadayar, C. Bäuerle, and T. Meunier, "Electrons surfing on a sound wave as a platform for quantum optics with flying electrons," Nature **477**, 435–438 (2011).

[5]P. Wang, L. Lu, and K. Bertoldi, "Topological Phononic Crystals with One-Way Elastic Edge Waves," Phys. Rev. Lett. **115**, 104302 (2015).

[6]W. Saad, M. Bennis, and M. Chen, "A Vision of 6G Wireless Systems: Applications, Trends, Technologies, and Open Research Problems," IEEE Network **34**, 134–142 (2020).

[7]L. Zheng, D. Wu, X. Wu, and K. Lai, "Visualization of Surface-Acoustic-Wave Potential by Transmission-Mode Microwave Impedance Microscopy," Phys. Rev. Applied **9**, 061002 (2018).

[8]L. Zheng, L. Shao, M. Loncar, and K. Lai, "Imaging Acoustic Waves by Microwave Microscopy: Microwave Impedance Microscopy for Visualizing Gigahertz Acoustic Waves," IEEE Microw. Mag. **21**, 60–71 (2020).

[9]D. Lee, Q. Liu, L. Zheng, X. Ma, H. Li, M. Li, and K. Lai, "Direct Visualization of Gigahertz Acoustic Wave Propagation in Suspended Phononic Circuits," Phys. Rev. Applied **16**, 034047 (2021).

[10]D. Lee, S. Meyer, S. Gong, R. Lu, and K. Lai, "Visualization of acoustic power flow in suspended thin-film lithium niobate phononic devices," Appl. Phys. Lett. **119**, 214101 (2021).

[11]L. Shao, D. Zhu, M. Colangelo, D. Lee, N. Sinclair, Y. Hu, P. T. Rakich, K. Lai, K. K. Berggren, and M. Lončar, "Electrical control of surface acoustic waves," Nat. Electron. **5**, 348–355 (2022).

[12]Q. Zhang, D. Lee, L. Zheng, X. Ma, S. I. Meyer, L. He, H. Ye, Z. Gong, B. Zhen, K. Lai, and A. T. C. Johnson, "Gigahertz topological valley Hall effect in nanoelectromechanical phononic crystals," Nat. Electron. **5**, 157–163 (2022).

[13]Y. Nii and Y. Onose, "Imaging an Acoustic Topological Edge Mode on a Patterned Substrate with Microwave Impedance Microscopy," Phys. Rev. Applied **19**, 014001 (2023).

[14]Y. Shi, J. Kahn, B. Niu, Z. Fei, B. Sun, X. Cai, B. A. Francisco, D. Wu, Z.-X. Shen, X. Xu, D. H. Cobden, and Y.-T. Cui, "Imaging quantum spin Hall edges in monolayer WTe2," Sci. Adv. **5**, eaat8799 (2019).

[15]M. E. Barber, E. Y. Ma, and Z.-X. Shen, "Microwave impedance microscopy and its application to quantum materials," Nat. Rev. Phys. **4**, 61–74 (2022).

[16]J.-Y. Shan, A. Pierce, and E. Y. Ma, "Universal signal scaling in microwave impedance microscopy," Appl. Phys. Lett. **121**, 123507 (2022).

[17]Y.-T. Cui, E. Y. Ma, and Z.-X. Shen, "Quartz tuning fork based microwave impedance microscopy," Rev. Sci. Instrum. **87**, 063711 (2016).

[18]Y. Yang, K. Lai, Q. Tang, W. Kundhikanjana, M. A. Kelly, K. Zhang, Z.-x. Shen, and X. Li, "Batch-fabricated cantilever probes with electrical shielding for nanoscale dielectric and conductivity imaging," J. Micromech. Microeng. **22**, 115040 (2012).

[19]D. M. Pozar, *Microwave Engineering*, 4th ed. (Wiley, Hoboken, NJ, 2011).

[20]M. Cai, O. Painter, and K. J. Vahala, "Observation of Critical Coupling in a Fiber Taper to a Silica-Microsphere Whispering-Gallery Mode System," Phys. Rev. Lett. **85**, 74–77 (2000).

[21]H. Kim, H. Choi, S. Jeon, and H. Kim, "Critical coupling of a planar inverted F-antenna using a ferrite sheet," Microw. Opt. Technol. Lett. **52**, 400–403 (2010).